






As a Matter of Dynamical Range – Scale Dependent Energy Dynamics in MHD Turbulence

Philipp Grete^{1,2} , Brian W. O’Shea^{2,3,4} , and Kris Beckwith⁵ ¹ Hamburger Sternwarte, Universität Hamburg, Gojenbergsweg 112, D-21029, Hamburg, Germany; pgrete@hs.uni-hamburg.de² Department of Physics and Astronomy, Michigan State University, East Lansing, MI 48824, USA³ Department of Computational Mathematics, Science and Engineering, Michigan State University, East Lansing, MI 48824, USA⁴ Facility for Rare Isotope Beams, Michigan State University, East Lansing, MI 48824, USA⁵ Sandia National Laboratories, Albuquerque, NM 87185-1189, USA*Received 2022 November 1; revised 2022 December 20; accepted 2022 December 20; published 2023 January 12*

Abstract

Magnetized turbulence is ubiquitous in many astrophysical and terrestrial plasmas but no universal theory exists. Even the detailed energy dynamics in magnetohydrodynamic (MHD) turbulence are still not well understood. We present a suite of subsonic, super-Alfvénic, high plasma beta MHD turbulence simulations that only vary in their dynamical range, i.e., in their separation between the large-scale forcing and dissipation scales, and their dissipation mechanism (implicit large eddy simulation, ILES, and direct numerical simulation (DNS)). Using an energy transfer analysis framework we calculate the effective numerical viscosities and resistivities, and demonstrate that all ILES calculations of MHD turbulence are resolved and correspond to an equivalent visco-resistive MHD turbulence calculation. Increasing the number of grid points used in an ILES corresponds to lowering the dissipation coefficients, i.e., larger (kinetic and magnetic) Reynolds numbers for a constant forcing scale. Independently, we use this same framework to demonstrate that—contrary to hydrodynamic turbulence—the cross-scale energy fluxes are not constant in MHD turbulence. This applies both to different mediators (such as cascade processes or magnetic tension) for a given dynamical range as well as to a dependence on the dynamical range itself, which determines the physical properties of the flow. We do not observe any indication of convergence even at the highest resolution (largest Reynolds numbers) simulation at 2048^3 cells, calling into question whether an asymptotic regime in MHD turbulence exists, and, if so, what it looks like.

Unified Astronomy Thesaurus concepts: [Magnetohydrodynamical simulations \(1966\)](#); [Magnetohydrodynamics \(1964\)](#); [Plasma astrophysics \(1261\)](#); [Magnetic fields \(994\)](#); [Theoretical techniques \(2093\)](#); [Computational methods \(1965\)](#)


Supporting material: [tar.gz file](#)

1. Introduction

Many astrophysical and terrestrial systems are turbulent and threaded by magnetic fields and as such, the dynamics in these systems are often described or modeled in the context of magnetohydrodynamic (MHD) turbulence. Astrophysical examples range from energy transport in the solar convection zone (Canuto & Christensen-Dalsgaard 1998; Miesch 2005) to star-forming molecular clouds (Falgarone et al. 2015; Vázquez-Semadeni 2015) to clusters of galaxies (Brüggen & Vazza 2015; Brunetti & Jones 2015) and angular momentum transport in accretion disks (Balbus & Hawley 1998). Terrestrial examples include plasma experiments, such as laser-produced colliding plasma flows, Z-pinches, and tokamaks (see, e.g., Haines 2011; Tzeferacos et al. 2018). In the absence of full 4D (spatial plus temporal) information, observations (astrophysical and laboratory experiments) often rely on MHD turbulence simulations to support interpretations. Similarly, numerical simulations are also frequently employed to support the development of MHD turbulence theories, which, in turn are also used to interpret observations. This illustrates the tight link between experiments/observations, numerical simulations, and theory.

Figure 1 illustrates some key properties of the canonical (incompressible) hydrodynamic turbulence phenomenology. Energy injected on the largest scales in a system is transferred conservatively in a self-similar cascade to smaller and smaller scales until it is dissipated on the smallest scales. On the intermediate range of scales associated with the cascade the energy spectrum (top panel of Figure 1) is a power law with a $k^{-5/3}$ slope and the energy flux across scales (center panel) is constant. With an increasing Reynolds number ($Re = UL/\nu \gtrsim 1000$) this intermediate (inertial) range between production/injection and dissipation scales, i.e., the dynamical range,⁶ becomes more and more extended while the spectral slope and energy flux remain constant. This phenomenology is in agreement with theory (Kolmogorov 1941; Frisch 1995) and has been confirmed in many experiments (both laboratory and numerical; e.g., Ishihara et al. 2016).

While the kinetic energy cascade is the only available energy transfer channel in incompressible hydrodynamic turbulence, the situation is significantly more complex for MHD turbulence. In MHD turbulence additional channels exist that also allow for a cascade of magnetic energy as well as transfer of energy between kinetic and magnetic energy budgets (Alexakis et al. 2005; Grete et al. 2017; Verma 2019). This complication is likely one reason for the lack of a “universal”

 Original content from this work may be used under the terms of the [Creative Commons Attribution 4.0 licence](#). Any further distribution of this work must maintain attribution to the author(s) and the title of the work, journal citation and DOI.

⁶ In this paper, we will use “dynamical range” interchangeably with the kinetic (and magnetic) Reynolds number.

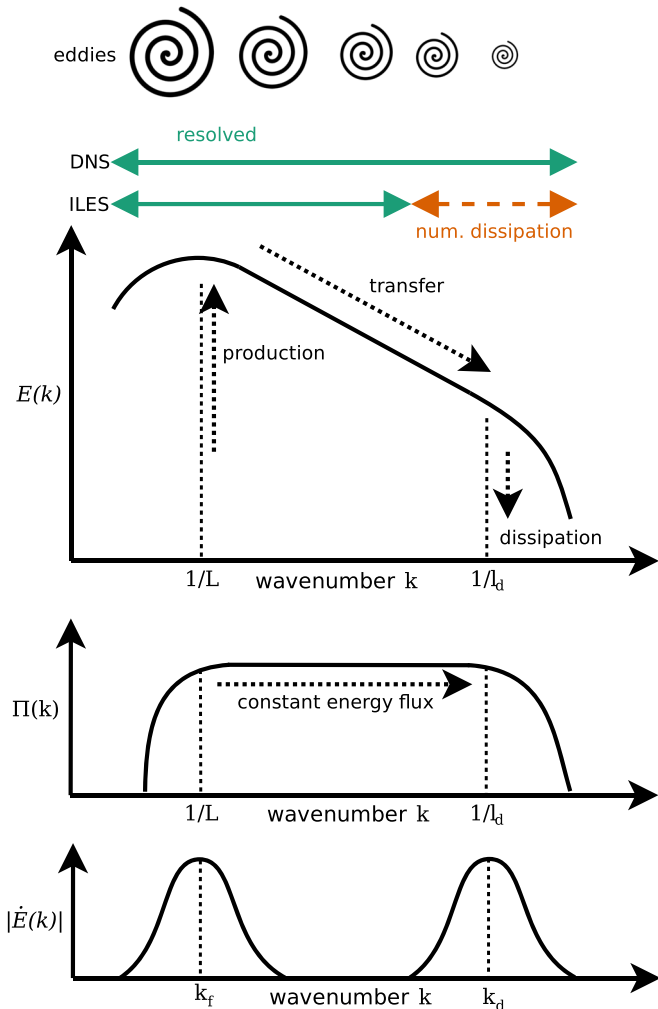


Figure 1. Illustrative sketches of the energy spectrum (top), cross-scale energy flux (middle), and absolute rate of change in energy (bottom) for idealized turbulence. Energy is injected to the system on the largest scales (in our simulations through a mechanical stochastic forcing process) resulting in large-scale eddies. Phenomenologically, these eddies break up into smaller and smaller eddies transferring energy to smaller scales at a constant energy flux on intermediate scales. At the smallest scales energy is dissipated. In direct numerical simulations (DNSs) the dissipative scales are resolved whereas in implicit large eddy simulation (ILES) dissipation is numerical in nature. In the stationary regime, the system is in balance, i.e., the integrated rate of change in energy injected to the system (bottom left) corresponds to the energy being dissipated (bottom right).

theory of MHD turbulence (see Beresnyak 2019; Schekochihin 2022, for recent reviews) and the existence of different competing theories, (e.g., for the slope of the energy spectra; see, e.g., Iroshnikov 1964; Kraichnan 1965; Goldreich & Sridhar 1995; Boldyrev et al. 2009).

For many astrophysical systems (such as the intracluster medium (ICM) and black hole accretion disks), direct numerical simulations (DNSs) that resolve from the largest scales in the system (see top of Figure 1) down to the (microphysical) dissipation scale are computationally intractable. Because of the large (magnetic) Reynolds numbers associated with these systems, such astrophysical plasmas have been traditionally studied using the equations of ideal MHD, which neglect both viscosity and resistivity. However, simulations of these systems have been performed using algorithms that apply artificial dissipation for stabilization, e.g.,

historically, the Method-of-Characteristics Constrained Transport algorithm (Hawley & Stone 1995) and more recently, Godunov-type finite volume methods (Stone et al. 2008). These choices firmly place ideal MHD turbulence simulations that utilize these algorithms in the realm of implicit large eddy simulations (ILESs; Grinstein et al. 2007).⁷ However, ILESs have no intrinsic notion of physical scales (e.g., with respect to the dissipative transport coefficients), which can lead to an expectation that the effective viscosity (and resistivity) depend on the number of grid points used for the simulation, or alternatively, that the effective viscosity (and resistivity) is fixed for a given cell width, Δ_x , and does not depend on the physical scales.

In this paper, we examine the physical interpretation of increasing the separation between the energy injection scale and the dissipation scale (the “dynamical range”) in implicit large eddy simulations of ideal MHD turbulence. This is accomplished through the analysis of a series of ILES calculations of MHD turbulence where we systematically vary the dynamical range and study the response of both the scale-wise distribution of energy and the physical mechanisms by which energy is transferred between scales in the turbulence. Based on this analysis, we demonstrate that, for the choice of magnetic field topology and numerical scheme considered here, the separation between the energy injection scale and the dissipation scale of ILES calculations of MHD turbulence determines the gross energetics of the flow. Through analysis of the dissipation mechanisms present in the calculations, we further demonstrate that the properties of ILES calculations of MHD turbulence accurately reproduces those of DNS calculations of visco-resistive MHD turbulence where the dissipation scale is well resolved. The combination of these two results leads us to the conclusion that all ILES calculations of MHD turbulence are *resolved* and correspond to an equivalent DNS calculation of visco-resistive MHD turbulence for a specific combination of magnetic field topology, energy injection scales, and dissipation coefficients. As a consequence, increasing the number of grid points used in an ILES calculation of MHD turbulence increases both the dynamical range of the calculation and also the effective (magnetic) Reynolds number. For ILES calculations of MHD turbulence, therefore, a correspondence exists between the dynamical range and effective (magnetic) Reynolds number and as such, increasing the dynamical range allows study of the asymptotic properties of MHD turbulence with the (magnetic) Reynolds number.

The rest of this paper is organized as follows. In Section 2, we describe the details of the MHD turbulence simulations performed here and the energy transfer analysis framework used to postprocess the data. In Section 3, we describe the energetic properties of the simulations, subsequent to which, we compare properties of the dissipation in the ILES and DNS simulations in Section 4. Finally, we summarize the key results of this work, draw conclusions, and point the way to future work in Section 5.

⁷ More recently, large eddy simulations that only resolve the largest scales directly and rely on a model to incorporate effects from the unresolved scales (e.g., dissipative processes acting on the smallest scales) have come into use (Sagaut 2006; Schmidt 2015).

Table 1
Overview of the Simulation Parameters and Properties in the Stationary Regime Analyzed in this Paper

Id	k_f	$\nu[10^{-4}]$	$\eta[10^{-4}]$	$\langle Ms \rangle$	$\langle Ma \rangle$	$\langle \beta_p \rangle$	k_d	$L_{int,U}$	$\langle Re \rangle$	$\langle Rm \rangle$	$\langle Pm \rangle$
N128_k2_ILES	2	2.78	2.66	0.57(1)	5.2(3)	150(12)	25	0.35	717	752	1.0
N256_k2_ILES	2	1.23	0.98	0.557(7)	4.6(2)	122(9)	42	0.34	1546	1943	1.3
N512_k2_ILES	2	0.53	0.36	0.54(1)	3.4(1)	75.0(2.9)	70	0.33	3389	4983	1.5
N1024_k2_ILES	2	0.23	0.15	0.55(2)	3.2(2)	63.6(2.5)	140	0.33	8030	12147	1.5
N2048_k2_ILES	2	0.10	0.06	0.551(5)	2.86(4)	53.4(7)	236	0.32	18571	27677	1.5
N1024_k4_ILES	4	0.27	0.19	0.598(5)	3.50(6)	63.6(1.6)	140	0.21	4688	6710	1.4
N2048_k8_ILES	8	0.562(3)	3.31(3)	64.0(1.5)	280	0.1
N512_k2_aDNS	2	1.20	0.98	0.561(5)	5.1(1)	151(5)	35	0.36	1421	1768	1.2
N1024_k2_DNS	2	1.20	0.98	0.59(2)	6.0(5)	190(10)	42	0.35	1662	2036	1.2
N1024_k2_aDNS	2	0.25	0.25	0.414(8)	4.5(3)	221(18)	70	0.38	4603	5150	1.1

Note. For the ILES the viscous, ν , and resistive, η , coefficients are the result of the fitting procedure described in Section 4. Re and Rm are the integral scale ($L_{int,U}$) kinetic and magnetic Reynolds numbers. Angular brackets denote the temporal mean.

2. Numerical Details

In total, we conduct 10 driven, magnetized turbulence simulations with K -Athena⁸ (Grete et al. 2021) in the subsonic super-Alfvénic regime with varying resolution, forcing scale, and dissipation mechanism (explicit and implicit). All simulation use a second-order finite volume scheme consisting of a predictor-corrector Van Leer-type integrator, HLLD Riemann solver, piecewise linear reconstruction in the primitive variables, and constrained transport to ensure the divergence-free condition of the magnetic field (Stone & Gardiner 2009). The simulations are approximately isothermal using an ideal equation of state for a perfect gas with an adiabatic index of $\gamma = 1.0001$. We use a mechanical, stochastic forcing mechanism that evolves in space and time prescribed by an Ornstein–Uhlenbeck process (Schmidt et al. 2009; Grete et al. 2018). The acceleration field has an inverse parabolic shape in spectral space with a peak at the characteristic forcing wavenumber k_f , an autocorrelation time that corresponds to a large eddy turnover time, and a fixed power (i.e., the rms acceleration field is constant in each simulation). Each simulation starts with a weak magnetic field field configured as an axis aligned cylinder with radius $0.4L_{box}$ so that no field lines cross the triple periodic box. Thus, the initial field configuration corresponds to a “no-net-flux” scenario, or, in other words, there is no large-scale mean field in our simulations. All simulations evolve for 10 large-scale eddy turnover times and we collect statistics in the stationary regime over ≈ 10 snapshots spanning the last five turnover times.

The simulations can logically be split into three groups—see Table 1 for a detailed overview of simulation input parameters⁹ and resulting statistics in the stationary regime. All simulations are identified as N###_k#_TYPE with the first ### block corresponding to the resolution in (linear) number of grid cells, the k# block to the characteristic forcing scale, and TYPE to the simulation type. For example, N512_k2_ILES is an ILES using a grid with 512^3 cells and a forcing profile that peaks at $k_f = 2$.

The first group consist of five identical simulations (driven at the largest scales $k_f = 2$) that only vary in their resolution

ranging from 128^3 to 2048^3 cells. These simulation were conducted with K -Athena. They include no explicit dissipation and solely rely on numerical dissipation, i.e., they are ILESs. We refer to this group as the one with “varying dynamical range.”

The second group consists of three simulations with “constant dynamical range” but varying number of grid cells. More specifically, we again use K -Athena to conduct ILESs but change the characteristic forcing scale with resolution so that the scale separation remains constant, i.e., the 512^3 simulation is driven at $k_f = 2$, the 1024^3 simulation at $k_f = 4$, and the 2048^3 simulation at $k_f = 8$.

Finally, the third group consists of three additional simulations that include explicit viscosity and resistivity. The viscous and resistive coefficients are chosen to match the effective numerical dissipative coefficients and the simulation identifiers specify either DNS or aDNS (“almost” direct numerical simulation) as type; see Section 4 for details.

We postprocess all simulations using the shell-to-shell energy transfer analysis presented in Grete et al. (2017) and extend it here to also account for energy transfer by viscous and resistive dissipation.¹⁰ The basic framework is an extension of Alexakis et al. (2005) to the compressible regime; see also Dar et al. (2001), Domaradzki et al. (2010), Mininni (2011), Verma (2019), Yang (2019), and references therein. This kind of energy transfer analysis allows detailed quantification of the energy transfer from a source (some energy budget at some spatial scale Q) to a sink (some budget at some scale K) via a mediating process.

The energy transfers¹¹ are generally denoted by

$$\mathcal{T}_{XY}(Q, K) \quad \text{with } X, Y \in \{U, B\} \quad (1)$$

indicating energy transfer (for $\mathcal{T} > 0$) from shell Q of energy budget X to shell K of energy budget Y . In this paper, U and B refer to the kinetic and magnetic energy budgets, respectively. More specifically, the energy transfers for kinetic-to-kinetic (and magnetic-to-magnetic) transfers via advection and

⁸ K -Athena is a performance portable version of Athena++ using Kokkos (Edwards et al. 2014; Trott et al. 2022). It is available at <https://gitlab.com/pgrete/kathena> and commit e5faee49 was used in this work.

⁹ A sample input parameter file, `athinput.fmturb.N1024_k2_DNS`, is contained in the `data.tar.gz` package.

¹⁰ The framework is available at <https://github.com/pgrete/energy-transfer-analysis> and commit 59b36a7 was used here.

¹¹ In general, the definition of the energy transfer terms is not unique; for details and discussion of physical interpretation of the ones chosen in this paper, see Grete et al. (2017).

compression (typically associated with energy cascades) are

$$\mathcal{T}_{UU}(Q, K) = - \int \mathbf{w}^K \cdot (\mathbf{u} \cdot \nabla) \mathbf{w}^Q + \frac{1}{2} \mathbf{w}^K \cdot \mathbf{w}^Q \nabla \cdot \mathbf{u} dx \quad (2)$$

$$\mathcal{T}_{BB}(Q, K) = - \int \mathbf{B}^K \cdot (\mathbf{u} \cdot \nabla) \mathbf{B}^Q + \frac{1}{2} \mathbf{B}^K \cdot \mathbf{B}^Q \nabla \cdot \mathbf{u} dx \quad (3)$$

where we use the mass-weighted velocity $\mathbf{w} = \sqrt{\rho} \mathbf{u}$ ensuring that the spectral kinetic energy density based on $\frac{1}{2} \mathbf{w}^2$ is positive definite (Kida & Orszag 1990). The magnetic-to-kinetic (and kinetic-to-magnetic) energy transfer via magnetic tension are

$$\mathcal{T}_{BUT}(Q, K) = \int \mathbf{w}^K \cdot (\mathbf{v}_A \cdot \nabla) \mathbf{B}^Q dx \quad (4)$$

$$\mathcal{T}_{UBT}(Q, K) = \int \mathbf{B}^K \cdot \nabla \cdot (\mathbf{v}_A \otimes \mathbf{w}^Q) dx \quad (5)$$

where \mathbf{v}_A is the Alfvén velocity. The magnetic-to-kinetic (and kinetic-to-magnetic) energy transfer via magnetic pressure are

$$\mathcal{T}_{BUP}(Q, K) = - \int \frac{\mathbf{w}^K}{2\sqrt{\rho}} \cdot \nabla (\mathbf{B} \cdot \mathbf{B}^Q) dx \quad (6)$$

$$\mathcal{T}_{UBP}(Q, K) = - \int \mathbf{B}^K \cdot \mathbf{B} \nabla \cdot \left(\frac{\mathbf{w}^Q}{2\sqrt{\rho}} \right) dx, \quad (7)$$

the internal-to-kinetic energy transfer via the pressure gradient (i.e., density fluctuations for the isothermal simulations used here¹²) is

$$\mathcal{T}_{PU}(Q, K) = - \int \frac{1}{\sqrt{\rho}} \mathbf{w}^K \cdot \nabla p^Q dx, \quad (8)$$

and the energy input from the mechanical forcing to the kinetic energy budget is given by

$$\mathcal{T}_{FU}(Q, K) = - \int \sqrt{\rho} \mathbf{w}^K \cdot \mathbf{a}^Q dx. \quad (9)$$

Finally, in this paper we expand the original, ideal framework with

$$\mathcal{T}_{\nu U}(Q, K) = \nu \int \sqrt{\rho} \mathbf{w}^K \cdot \left(\Delta \mathbf{u}^Q + \frac{1}{3} \nabla (\nabla \cdot \mathbf{u}^Q) \right) dx \quad (10)$$

$$\mathcal{T}_{\eta B}(Q, K) = \eta \int \mathbf{B}^K \cdot \Delta \mathbf{B}^Q dx \quad (11)$$

for viscous and resistive dissipation with coefficients ν and η , respectively.

Superscripts K and Q indicate shell-filtered quantities, e.g., \mathbf{w}^K is the velocity field on scales K or \mathbf{B}^Q is the magnetic field on scales Q . The scales are separated by a sharp spectral filter in Fourier space with logarithmic spacing.¹³ The bounds are given by 1 and $2^{n/4+2}$ for $n \in \{-1, 0, 1, \dots, 36\}$. Shells (uppercase, e.g., K) and wavenumbers (lowercase, e.g., k) obey a direct mapping, i.e., $K = 24$ corresponds to $k \in (22.6, 26.9]$.

From the individual transfer terms, several aggregated quantities can be derived that are often used in turbulence studies. This includes the cross-scale fluxes that are generically

¹² For a detailed analysis including the internal energy budget see Schmidt & Grete (2019) or Grete et al. (2020) for non-isothermal statistics.

¹³ In the subsonic regime of the simulations presented in this paper density variations are limited. Therefore, differences between shell-filtered transfers and transfers calculated using a coarse-graining approach as in large eddy simulations are expected to be negligible (Aluie 2013; Yang et al. 2016; Zhao & Aluie 2018).

given by

$$\Pi_{Y>}^{X<}(k) = \sum_{Q \leq k} \sum_{K > k} \mathcal{T}_{XY}(Q, K) \quad (12)$$

and quantify how much energy is transferred across a reference scale k from all scales larger than k in budget X to all scales smaller than k in budget Y; see center panel in Figure 1. For ease of comparison, the energy transfer terms are typically normalized so that the total cross-scale flux (including all terms) is unity on intermediate (inertial) scales, which we also follow in this paper.

Similarly, the rate of change in energy at some scale (here, in some energy bin K) from a given term $\mathcal{T}_{XY}(Q, K)$ can be computed from

$$\dot{E}_{XY}(K) = \sum_Q \mathcal{T}_{XY}(Q, K). \quad (13)$$

The total rate of change (including all terms) vanishes on average for stationary turbulence by construction; see bottom panel of Figure 1.

3. Properties of MHD Turbulence in Implicit Large Eddy Simulations

The (temporal) mean kinetic and magnetic energy spectra for ILESs with fixed forcing scale, $k_f = 2$, but increasing resolution (128^3 to 2048^3) are shown in the left panels of Figure 2. This plot can be interpreted as a prototypical numerical convergence plot as all parameters except for the number of grid cells (or Δ_x) are kept constant. The large-scale kinetic energy spectra of all simulations are effectively identical. At the same time, an increased resolution (smaller Δ_x) results in an extended range where the kinetic energy spectrum follows a power law. The latter scales with $\approx k^{-4/3}$, which has been observed before (Haugen et al. 2004; Aluie & Eyink 2010; Moll et al. 2011; Teaca et al. 2011; Porter et al. 2015; Grete et al. 2017; Bian & Aluie 2019; Glines et al. 2021) and that we attribute to magnetic tension being dominant on those scales (Grete et al. 2021). While the magnetic energy spectrum also becomes more and more extended with larger dynamical range, no power-law regime is observed even at the highest resolution.

At first glance, this extension of the spectra toward smaller scales with increasing resolution may be simply interpreted as an extension of the overall dynamics on smaller scales with no impact on the intermediate or larger scales.

An alternative illustration of this same data is shown in the center panels of Figure 2, which show the same spectra as in the left panels but with the x -axis normalized to the peak dissipation scale (see the bottom panel of the sketch in Figure 1) instead of the forcing scale. Both kinetic and magnetic energy spectra are well aligned across all simulations on scales $k \gtrsim k_d$ but are neither ‘‘converged’’ on intermediate nor large scales, that is, $k \lesssim k_d$. That the small-scale behavior is well aligned is explored further in the data shown in the right-hand panels of Figure 2, which again show the mean kinetic and magnetic energy spectra for ILESs with varying resolution (512^3 , 1024^3 , and 2048^3 grid cells), but with the forcing scale adjusted accordingly from $k_f = 2$, to $k_f = 4$, to $k_f = 8$, respectively. As a result, the dynamical range given by the separation between the energy injection scale and the (numerical) dissipation scale is kept constant in these simulations. Both the kinetic and magnetic energy spectra are

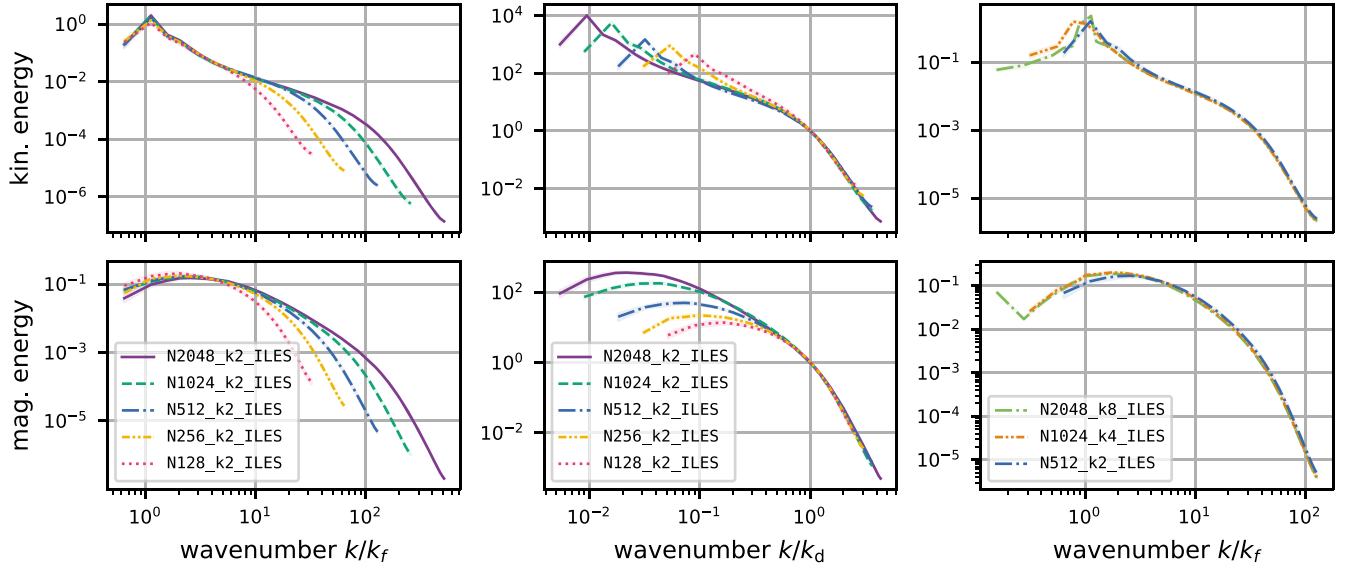


Figure 2. Mean kinetic (top) and magnetic (bottom) energy spectra in the stationary regime for simulations with varying dynamical range (left panels with the x -axis scaled to the forcing scale, k_f , and center panels scaled to the peak dissipative scale, k_d) and fixed dynamical range but varying resolution (right). The left and right spectra are normalized to the mean energy between $1.5k_f \leq k \leq 6k_f$ and the center spectra are normalized to unity at k_d . The (barely visible) shaded regions show the standard deviation of the spectra over time.

effectively identical for all simulations across the shared scales (smaller than the forcing scale). The data of the right-hand panel of Figure 2 demonstrate one of the key results of this work: the separation between the energy injection scale and the dissipation scale, which we term the dynamical range, rather than the number of grid points or the grid spacing, Δ_x , determines the spectral energy distribution within the turbulence.

The next step in our analysis involves understanding how the dynamical range determines the physical mechanisms by which energy is transferred across scales in the turbulence. The data of the left-hand panels of Figure 3 show the key channels, i.e., the kinetic, $\Pi_{U>}^{U<}$, and magnetic, $\Pi_{B>}^{B<}$, cascades and the magnetic-to-kinetic cross-scale flux via magnetic tension, $\Pi_{U>}^{B<,T}$ and vice versa, $\Pi_{B>}^{U<,T}$, for the simulations with fixed forcing at $k_f=2$ and varying dynamical range. The data of this figure show that no individual cross-scale flux is constant over any range of scales in any simulation, in stark contrast to (incompressible) hydrodynamic turbulence where the kinetic cascade flux is constant in the inertial range. For the ILES-based MHD turbulence calculations shown in left-hand panels of Figure 3, this applies only to the total flux, i.e., the one taking all terms into account simultaneously (see bottom left panel of Figure 3).

Next, all cross-scale fluxes vary with number of grid cells and the dominant channel becomes a function of scale and dynamical range. For example, at the lowest resolution the kinetic cascade cross-scale flux is a continuously decreasing function with smaller scales (red dotted line in top left panel of Figure 3) whereas at resolutions $\gtrsim 1024^3$ cells the cross-scale flux exhibits a local peak around $\approx 0.8k_d$ before declining again and even reaching negative values (i.e., a flux of energy to larger scales) on intermediate scales. Similarly, the kinetic-to-magnetic cross-scale flux via magnetic tension peaks at ≈ 0.5 at 128^3 and with increasing resolution the peak becomes more dominant and shifts toward larger scales following the forcing scale. In other words, at the lowest resolution about one half of the cross-scale flux from the large-scale kinetic budget goes to

each the kinetic and magnetic budget on smaller scales whereas at the highest resolution $\approx 80\%$ end up on smaller magnetic scales with diminishing contributions to the kinetic energy budget on smaller scales.

For the simulations with identical dynamical range the individual cross-scale fluxes are also a function of wavenumber but they are identical between the simulations with different Δ_x ; see right panels in Figure 3. This result is similar to that obtained for the energy spectra and indicates that the physics of energy transfer is determined by the dynamical range, rather than the number of grid points for ILES calculations.

4. Comparing Magnetohydrodynamic ILES and DNS Calculations: Properties of Numerical Dissipation

In the previous section, we have seen that both the spectral energy distribution and the mechanisms by which energy is transferred between scales in ILES calculations of MHD turbulence are determined by the dynamical range of the calculation, rather than, e.g., the number of grid points. In this section, we analyze the properties of the numerical dissipation in these calculations and compare the results of this analysis to an equivalent set of DNS calculations.

The scale-wise rate of change in the kinetic and magnetic energy budget are given by (see also, e.g., Simon et al. 2009; Salvesen et al. 2014)

$$\partial_t E_{\text{kin}}^K = \int_Q \sum (\mathcal{T}_{UU} + \mathcal{T}_{\text{BUT}} + \mathcal{T}_{\text{BUP}} + \mathcal{T}_{\text{PU}} + \mathcal{T}_{\text{FU}} + \mathcal{T}_{\nu U}) dx + D_U \quad (14)$$

$$\partial_t E_{\text{mag}}^K = \int_Q \sum (\mathcal{T}_{\text{BB}} + \mathcal{T}_{\text{UBT}} + \mathcal{T}_{\text{UBP}} + \mathcal{T}_{\eta B}) dx + D_B. \quad (15)$$

For stationary turbulence $\partial_t E_{\text{kin}}^K = \partial_t E_{\text{mag}}^K = 0$ must hold on average by definition as the system is in global balance. In ILESs, the dissipative terms, $\mathcal{T}_{\nu U}$ and $\mathcal{T}_{\eta B}$, are absent and \mathcal{D} represents the numerical dissipation in the kinetic and magnetic energy. By contrast, the dissipative scales (and, thus, $\mathcal{T}_{\nu U}$ and

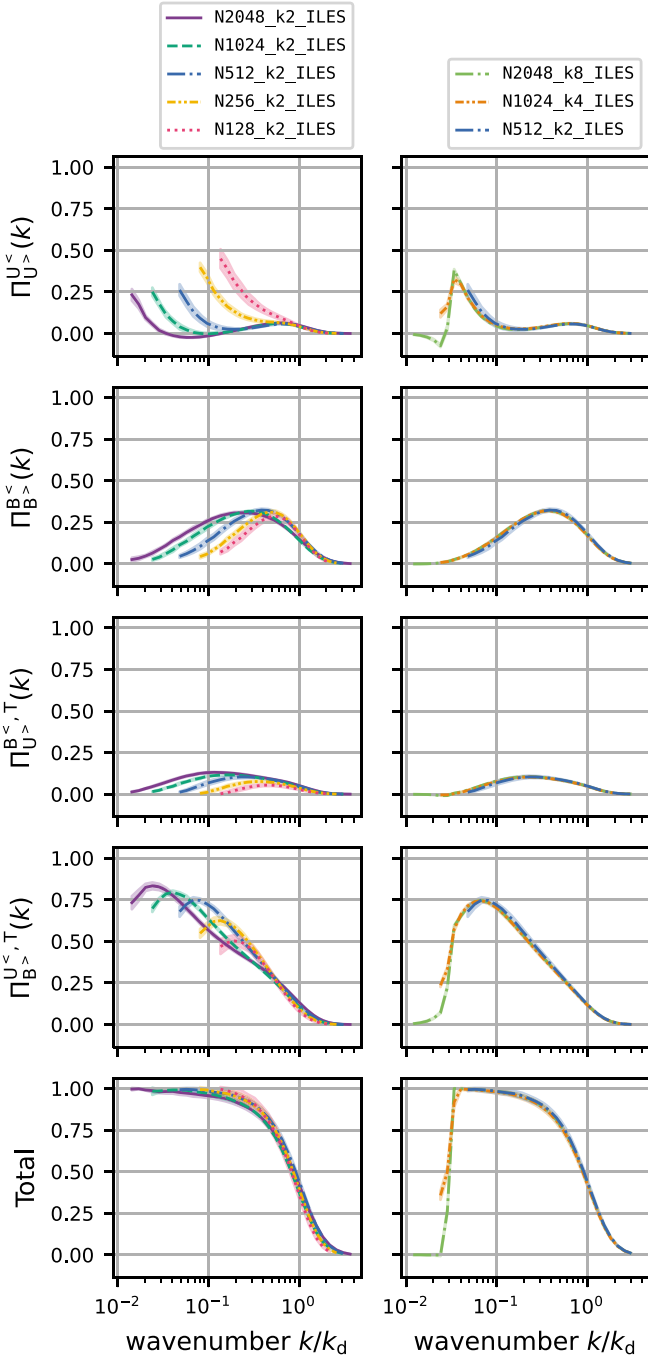


Figure 3. Mean cross-scale fluxes of the simulations with varying dynamical range (left) and identical range but varying resolution (right) for, from top to bottom, kinetic-to-kinetic, magnetic-to-magnetic, magnetic-to-kinetic via magnetic tension, kinetic-to-magnetic via magnetic tension, and all-to-all (total) energy fluxes.

$\mathcal{T}_{\eta B}$) are fully resolved in DNSs and $\mathcal{D} = 0$. This is illustrated in Figure 4. The blue line in each panel shows the temporal mean total rate of change ($\partial_t E_{\text{kin}}^K + \partial_t E_{\text{mag}}^K$) for an ILES (top), an almost-resolved DNS (center), and a DNS (bottom). As expected, it vanishes for the DNS as all transfers are explicitly accounted for and exhibits a pronounced peak reaching ≈ 0.1 in the ILES as numerical dissipation is not explicitly accounted for. In the center panel it still reaches ≈ 0.025 despite the dissipative terms being included in the simulation. This indicates that $\mathcal{T}_{\nu U}$ and $\mathcal{T}_{\eta B}$ are not fully resolved and a small

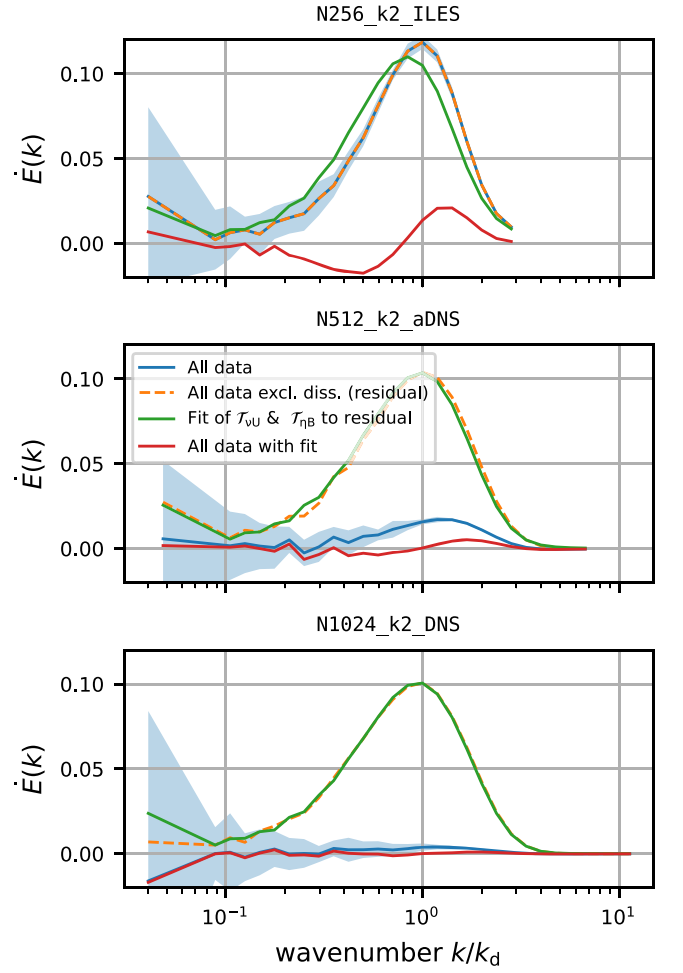


Figure 4. Fitting the rate of change in energy from the dissipative transfer terms, $\mathcal{T}_{\nu U}$ and $\mathcal{T}_{\eta B}$, to the residual in an ILES (top), an almost-resolved DNS (center), and a DNS (bottom). For the DNS the residual is calculated from all fluxes excluding the dissipative terms whereas in the ILES the residual is a true residual from the analysis.

amount of numerical dissipation remains. Therefore, we identify this simulation as an “almost” DNS.

In addition to determining if a simulation is resolved, this analysis also allows estimation of the numerical dissipative coefficients by fitting to the residuals of the net rate of change. More specifically, we calculate both the scale-wise residual numerical dissipation, e.g.,

$$\mathcal{D}_B(K) = - \int \sum_Q (\mathcal{T}_{BB} + \mathcal{T}_{UBT} + \mathcal{T}_{UBP}) dx \quad (16)$$

and the expected resistive dissipation $\int \sum_Q (\mathcal{T}_{\eta B}) dx$ and eventually apply a linear least square method to determine the effective η ; we apply the same methodology to compute the viscosity as well. The joint (kinetic plus magnetic) residual is shown as orange dashed line in Figure 4. For ILESs it is identical to the blue “all data” line as the dissipative terms are only included in the postprocessing described here but not in the simulations themselves. For the two DNS calculations, we specifically exclude the dissipative terms to calculate the residual. This allows for a sanity check of the procedure if the original coefficients included in the simulations can be recovered. The result of the parameter estimation is illustrated

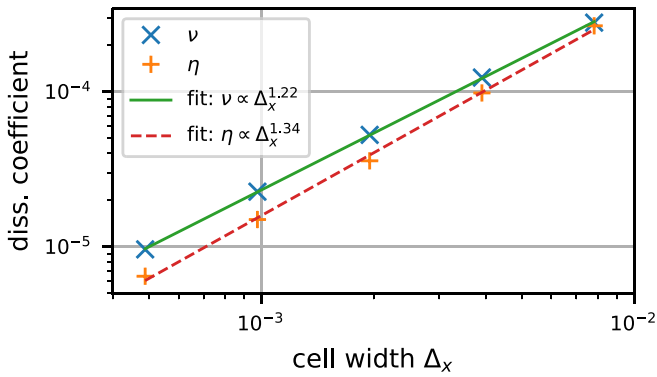


Figure 5. Calculated effective ν and η in the ILES with large-scale forcing and varying resolution (cell width Δ_x) and power-law fits to the data.

by the green lines in Figure 4. The DNS coefficients are recovered exactly (the green and orange line are on top of each other) and for the ILES we report the results of the fitting in Table 1. In general, for the ILES a significant fraction of the residual is accounted for by the fit; see the red line in Figure 4 that shows the overall residual including the dissipative terms with the estimated coefficient. However, the peak of the original residual (blue/orange) and the dissipative terms are not aligned on the x -axis. This mismatch in alignment cannot be fixed by the fitting as it only scales the data in the y -direction. This indicates that the numerical dissipation of the scheme employed in the simulations here largely acts similar to standard viscous and resistive dissipation but contains some small level of higher-order terms that act to push the maximum numerical dissipation to smaller scales. The calculated effective ν and η for the ILES with large-scale forcing and varying resolution (cell width Δ_x) are shown in Figure 5. Both coefficients follow power laws that scale with $\nu \propto \Delta_x^{1.22}$ and $\eta \propto \Delta_x^{1.34}$, respectively.

The three DNSs presented in the preceding subsection were not chosen at random. In fact, we first analyzed the existing N256_k2_ILES and N512_k2_ILES simulations to determine the effective viscous and resistive coefficients. Afterwards, we conducted the three DNSs using those coefficients but at higher resolutions. More specifically, we used the effective dissipative coefficients of the N256_k2_ILES simulation for N512_k2_aDNS and N512_k2_DNS, and the effective coefficients from N512_k2_ILES for N1024_k2_aDNS. Figure 6 illustrates the cross-scale fluxes of the two ILESs along the three DNSs. Again, the results from simulations with the same dynamical range fall on top of each other irrespective of whether the dissipative processes are included explicitly or implicitly. This naturally includes the scale-wise variations observed and discussed for ILESs previously, i.e., there exists no range over which the individual cross-scale fluxes are constant and the physics of the turbulence is independent of the numerical methodology employed. In other words, the effective numerical dissipation utilized in the ILES calculations presented here are well suited to approximate DNS turbulence simulations. From this, we conclude that the scale-dependent cross-scale fluxes are not tied to the numerical dissipation utilized in the ILES results presented here and are consistent with the scale-dependent cross-scale fluxes derived from higher-resolution DNS calculations at a specified set of

(magnetic) Reynolds numbers. In other words, ILESs performed at a given dynamical range provides a *converged* representation of DNSs for a specific choice of energy injection scale, and dissipation coefficients (e.g., magnetic Reynolds number). If the dynamical range of an ILES calculation is varied (e.g., increased by adding additional grid points), then the DNS calculation that this represents also changes, through, e.g., an increased (magnetic) Reynolds number.

5. Summary, Discussion, and Conclusions

Motivated by earlier results on the different scaling of kinetic and magnetic energy spectra in MHD turbulence (Glins et al. 2021; Grete et al. 2021), we applied a shell-to-shell analysis framework to simulations in the same subsonic, super-Alfvénic driven MHD turbulence regime but with varying dynamical range and with or without explicit viscosity and resistivity. Simulations with explicit dissipative terms are DNSs and simulations that rely on the numerical method for dissipation are so-called ILESs. We conducted a range of ILES calculations where we varied the resolution (from 128^3 to 2048^3 grid cells) and the ratio between the energy injection scale and the dissipation scale (the “dynamical range”). The key results from this study can be summarized as follows:

1. The dynamical range, rather than the number of grid points or the grid spacing, Δ_x , determines both the spectral energy distribution and the physics of energy transfer between scales within ILES-based MHD turbulence.
2. Cross-scale energy fluxes in ILES-based MHD turbulence vary both with scale and dynamical range—even in the “inertial range” and in contrast to hydrodynamic turbulence.
3. The properties of numerical dissipation determined by the energy transfer analysis framework within ILES-based MHD turbulence is well modeled by standard visco-resistive dissipation term on a scale-wise basis in the steady state. For the ILES models presented here, the effective numerical viscosity and resistivity scale with $\nu \propto \Delta_x^{1.22}$ and $\eta \propto \Delta_x^{1.34}$, respectively.
4. DNSs and ILESs give effectively identical results at the same (effective) Reynolds numbers in terms of the physics of energy transfer between scales.

These results both have practical implications as well as raise important questions. First, as previously stated, ILESs performed at a given dynamical range provides a *converged* representation of DNSs for a specific choice of energy injection scale, and dissipation coefficients (e.g., magnetic Reynolds number). Studying the variation of ILES-based models of MHD turbulence with a changing dynamic range is equivalent to studying the variation of a set of DNS models with a changing (magnetic) Reynolds number, at least for the magnetic field topology considered here. Beyond this, our results give rise to the question of whether an asymptotic regime in MHD turbulence exists, and, if so, what are its properties. While in hydrodynamic turbulence an extended dynamical range simply leads to an extended power-law scaling in the kinetic energy spectrum and constant energy flux, we have not observed this behavior in the MHD turbulence simulations presented here. Even at the highest resolution with the largest dynamical range, both spectra and cross-scale fluxes still evolve and exhibit different (scale-wise) behavior

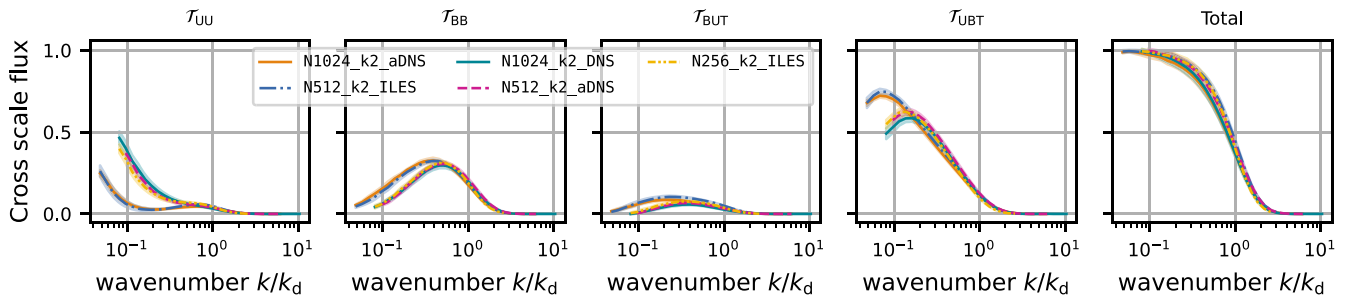


Figure 6. Mean (temporal) cross-scale fluxes of DNSs (with varying η and ν) and ILESs (with varying resolution).

compared to simulations with smaller dynamical range. MHD turbulence simulations are typically conducted with a dynamical range corresponding to Reynolds numbers of a few thousand whereas Reynolds numbers in many natural systems are expected to be significantly larger—especially in astrophysics. As an example of such behavior, in the ILES calculations with identical large-scale forcing presented here, the kinetic cascade cross-scale flux changes behavior between resolutions of $\leq 256^3$ and $\geq 512^3$ grid cells. The former fluxes are continuously decreasing functions of scale whereas the latter contain an inflection point, suggesting that the physics of turbulence at low Reynolds numbers is markedly different from that at high Reynolds numbers. We attribute this to magnetic tension that becomes more and more dynamically relevant with an increasing Reynolds number. In other words, at low Reynolds numbers the magnetic fields have not been amplified enough to be able to suppress the kinetic energy cascade in a substantial way; see Grete et al. (2021). This is also in agreement with recent results by Galishnikova et al. (2022) on a tearing-limited turbulent dynamo who also observe a change in behavior between low- and high-resolution simulations (comparable to the ones presented here). Thus, it will be very informative to analyze future simulations with (significantly) larger dynamic range to determine if this tearing-limited dynamo will result in an asymptotic regime.

The observed scaling of $\nu \propto \Delta_x^{1.22}$ has been reported before in forced, isotropic, hydrodynamic turbulence simulations; see Section III.A.2. in Zhou et al. (2014). Their estimation is based on large-scale quantities and assumes a developed inertial range. Therefore, it is encouraging that the procedure presented in this paper yields the same result without a clear scale separation (see the N128_k2_ILES simulation). Interestingly, Zhou et al. (2014) employed a spatially fourth-order accurate scheme contrary to the second-order accurate scheme here. At the same time, Salvesen et al. (2014) report lower effective viscosities and resistivities from simulations employing a spatially third-order scheme (but otherwise identical to the one here) using a procedure based on manually matching energy spectra between ILESs and DNSs. This motivates a more detailed study of the importance of (or lack thereof) the numerical scheme on both the effective dissipative coefficient values as well as their scaling.

Our results cover the subsonic, super-Alfvénic regime at a constant magnetic Prandtl number of approximately $\text{Pm} \approx 1$, i.e., the ratio of viscosity to resistivity is fixed, along with a specific choice of magnetic field topology and driving mechanism. From both a physical and a theoretical point of view, a larger parameter space covering the $\text{Pm} \gg 1$ and $\text{Pm} \ll 1$ should be explored in the future to evaluate how the energy dynamics change and if there are indications of

asymptotic behavior in those regimes. This similarly applies to systems with different Mach numbers, as for example, simulations performed at different Mach numbers (while maintaining a constant isothermal sound speed as in the simulations here) would directly translate to a varying Reynolds number. While we have used dynamical range and Reynolds number interchangeably in the text, this only applies to a set of simulations with constant characteristic velocity. However, we note that the physics of energy transfer also varies with Mach number, (see, e.g., Grete et al. 2017, for a side-by-side comparison of a sub- and supersonic MHD case). Therefore, a more complex relation between dynamical range and Reynolds number is expected (particularly in the supersonic regime), which should be explored in subsequent work.

While the determination of the effective numerical viscosity and resistivity was accurate for the simulations presented here, additional simulations are required to evaluate the applicability of the method, for example, in the highly supersonic regime where the impact of the numerical method (such as nonlinear limiters) is expected to be more pronounced. In addition to varying the Mach number of the flow, the nature of the driving mechanism should be explored. In particular, systems that are driven on all scales, such as accretion disks, where Keplerian shear can, in principle, inject energy into turbulence arising from the magnetorotational instability (Balbus & Hawley 1998) down to the viscous dissipation scale, could exhibit markedly different properties to the energy injection mechanisms studied here (see, e.g., Workman & Armitage 2008, for a discussion of potential issues here). Finally, different magnetic field topologies that vary both the amount of net flux threading the simulation domain and the magnetic helicity should be considered; such magnetic field configurations could influence the physics of energy transfer and lead to, e.g., inverse transfer of magnetic energy between scales, such as has been observed in recent experimental and computational work Ruiz et al. (2022).

This paper is dedicated to the memory of John Hawley (1958–2021), whose mentorship, guidance, and inspiration the authors are indebted to (see Balbus 2022). P.G. acknowledges funding from LANL through Subcontract No. 615487. This project has received funding from the European Union’s Horizon 2020 research and innovation program under the Marie Skłodowska-Curie grant agreement No. 101030214. Sandia National Laboratories is a multimission laboratory managed and operated by National Technology and Engineering Solutions of Sandia LLC, a wholly owned subsidiary of Honeywell International Inc., for the U.S. Department of Energy’s National Nuclear Security Administration under

contract DE-NA0003525. The views expressed in the article do not necessarily represent the views of the U.S. Department of Energy or the United States Government. SAND Number: SAND2022-13996 O. B.W.O. acknowledges support from NSF grants Nos. 1908109 and 2106575 and NASA ATP grants NNX15AP39G and 80NSSC18K1105.

The simulations and analysis were run on the NASA Pleiades supercomputer through allocation SMD-16-7720 and on TACC's Frontera supercomputer through LRAC allocation #AST20004 (Stanzione et al. 2020). The authors gratefully acknowledge the Gauss Centre for Supercomputing e.V. (www.Gauss-center.eu) for funding this project by providing computing time on the GCS Supercomputer JUWELS at Jülich Supercomputing Centre (JSC).

The software below is developed by a large number of independent researchers from numerous institutions around the world. Their commitment to open science has helped make this work possible.

Software: K-Athena (Grete et al. 2021), a performance portable version of Athena++ (Stone et al. 2020) using Kokkos (Edwards et al. 2014; Trott et al. 2022), Matplotlib (Hunter 2007), NumPy (van der Walt et al. 2011), mpi4py (Dalcin et al. 2005), mpi4py-fft (Dalcin et al. 2019).

ORCID iDs

Philipp Grete  <https://orcid.org/0000-0003-3555-9886>
 Brian W. O'Shea  <https://orcid.org/0000-0002-2786-0348>
 Kris Beckwith  <https://orcid.org/0000-0002-5610-8331>

References

- Alexakis, A., Mininni, P. D., & Pouquet, A. 2005, *PhRvE*, **72**, 046301
 Aluie, H. 2013, *PhyD*, **247**, 54
 Aluie, H., & Eyink, G. L. 2010, *PhRvL*, **104**, 081101
 Balbus, S. 2022, *NatAs*, **6**, 173
 Balbus, S. A., & Hawley, J. F. 1998, *RvMP*, **70**, 1
 Beresnyak, A. 2019, *LRCA*, **5**, 2
 Bian, X., & Aluie, H. 2019, *PhRvL*, **122**, 135101
 Boldyrev, S., Mason, J., & Cattaneo, F. 2009, *ApJL*, **699**, L39
 Brüggem, M., & Vazza, F. 2015, *Magnetic Fields in Diffuse Media* ed. A. Lazarian, M. E. de Gouveia Dal Pino, & C. Melioli (Berlin: Springer), 599
 Brunetti, G., & Jones, T. W. 2015, *Magnetic Fields in Diffuse Media* ed. A. Lazarian, M. E. de Gouveia Dal Pino, & C. Melioli (Berlin: Springer), 557
 Canuto, V. M., & Christensen-Dalsgaard, J. 1998, *AnRFM*, **30**, 167
 Carter Edwards, H. C., Trott, C. R., & Sunderland, D. 2014, *JPDC*, **74**, 3202
 Dalcin, L., Mortensen, M., & Keyes, D. E. 2019, *JPDC*, **128**, 137
 Dalcin, L., Paz, R., & Storti, M. 2005, *JPDC*, **65**, 1108
 Dar, G., Verma, M. K., & Eswaran, V. 2001, *PhyD*, **157**, 207
 Domaradzki, J. A., Teaca, B., & Carati, D. 2010, *PhFI*, **22**, 051702
 Falgarone, E., Momferratos, G., & Lesaffre, P. 2015, *Magnetic Fields in Diffuse Media* ed. A. Lazarian, M. E. de Gouveia Dal Pino, & C. Melioli (Berlin: Springer), 227
 Frisch, U. 1995, *Turbulence: The Legacy of AN Kolmogorov* (Cambridge: Cambridge Univ. Press)
 Galishnikova, A. K., Kunz, M. W., & Schekochihin, A. A. 2022, *PhRvX*, **12**, 041027
 Glines, F. W., Grete, P., & O'Shea, B. W. 2021, *PhRv*, **103**, 043203
 Goldreich, P., & Sridhar, S. 1995, *ApJ*, **438**, 763
 Grete, P., Glines, F. W., & O'Shea, B. W. 2021, *ITPDS*, **32**, 85
 Grete, P., O'Shea, B. W., & Beckwith, K. 2018, *ApJL*, **858**, L19
 Grete, P., O'Shea, B. W., & Beckwith, K. 2020, *ApJ*, **889**, 19
 Grete, P., O'Shea, B. W., & Beckwith, K. 2021, *ApJ*, **909**, 148
 Grete, P., O'Shea, B. W., Beckwith, K., Schmidt, W., & Christlieb, A. 2017, *PhPI*, **24**, 092311
 Grinstein, F., Margolin, L., & Rider, W. 2007, *Implicit Large Eddy Simulation: Computing Turbulent Fluid Dynamics* (Cambridge: Cambridge Univ. Press)
 Haines, M. G. 2011, *PPCF*, **53**, 093001
 Haugen, N. E. L., Brandenburg, A., & Dobler, W. 2004, *PhRvE*, **70**, 016308
 Hawley, J. F., & Stone, J. M. 1995, *CoPhC*, **89**, 127
 Hunter, J. D. 2007, *CSE*, **9**, 90
 Iroshnikov, P. S. 1964, *SvA*, **7**, 566
 Ishihara, T., Morishita, K., Yokokawa, M., Uno, A., & Kaneda, Y. 2016, *PhRvF*, **1**, 082403
 Kida, S., & Orszag, S. A. 1990, *JSCOM*, **5**, 85
 Kolmogorov, A. 1941, *DoSSR*, **30**, 301
 Kraichnan, R. H. 1965, *PhFI*, **8**, 1385
 Miesch, M. S. 2005, *LRSF*, **2**, 1
 Mininni, P. D. 2011, *AnRFM*, **43**, 377
 Moll, R., Pietarila Graham, J., Pratt, J., et al. 2011, *ApJ*, **736**, 36
 Porter, D. H., Jones, T. W., & Ryu, D. 2015, *ApJ*, **810**, 93
 Ruiz, D. E., Yager-Elorriaga, D. A., Peterson, K. J., et al. 2022, *PhRvL*, **128**, 255001
 Sagaut, P. 2006, *Large Eddy Simulation for Incompressible Flows: An Introduction, Scientific Computation* (Berlin: Springer)
 Salvesen, G., Beckwith, K., Simon, J. B., O'Neill, S. M., & Begelman, M. C. 2014, *MNRAS*, **438**, 1355
 Schekochihin, A. A. 2022, *JPIPh*, **88**, 155880501
 Schmidt, W. 2015, *LRCA*, **1**, 2
 Schmidt, W., Federrath, C., Hupp, M., Kern, S., & Niemeyer, J. C. 2009, *A&A*, **494**, 127
 Schmidt, W., & Grete, P. 2019, *PhRvE*, **100**, 043116
 Simon, J. B., Hawley, J. F., & Beckwith, K. 2009, *ApJ*, **690**, 974
 Stanzione, D., West, J., Evans, R. T., et al. 2020, in *PEARC '20: Practice and Experience in Advanced Research Computing* (New York: Association for Computing Machinery), 106
 Stone, J. M., & Gardiner, T. 2009, *NewA*, **14**, 139
 Stone, J. M., Gardiner, T. A., Teuben, P., Hawley, J. F., & Simon, J. B. 2008, *ApJS*, **178**, 137
 Stone, J. M., Tomida, K., White, C. J., & Felker, K. G. 2020, *ApJS*, **249**, 4
 Teaca, B., Carati, D., & Andrzej Domaradzki, J. 2011, *PhPI*, **18**, 112307
 Trott, C. R., Lebrun-Grandie, D., Arndt, D., et al. 2022, *ITPDS*, **33**, 805
 Tzeferacos, P., Rigby, A., Bott, A. F. A., et al. 2018, *NatCo*, **9**, 591
 van der Walt, S., Colbert, S. C., & Varoquaux, G. 2011, *CSE*, **13**, 22
 Vázquez-Semadeni, E. 2015, in *Magnetic Fields in Diffuse Media*, ed. A. Lazarian, M. E. de Gouveia Dal Pino, & C. Melioli (Berlin: Springer), 401
 Verma, M. K. 2019, *Energy Transfers in Fluid Flows: Multiscale and Spectral Perspectives* (Cambridge: Cambridge Univ. Press)
 Workman, J. C., & Armitage, P. J. 2008, *ApJ*, **685**, 406
 Yang, Y. 2019, *Energy Transfer and Dissipation in Plasma Turbulence* (Berlin: Springer), 69
 Yang, Y., Shi, Y., Wan, M., Matthaeus, W. H., & Chen, S. 2016, *PhRvE*, **93**, 061102
 Zhao, D., & Aluie, H. 2018, *PhRvF*, **3**, 054603
 Zhou, Y., Grinstein, F. F., Wachtor, A. J., & Haines, B. M. 2014, *PhRvE*, **89**, 013303